Inhomogeneous Kinetic Alfvén Waves in the Near-Sun Solar Wind

David M. Malaspina, Alexandros Chasapis, Peter Tatum, Chadi Salem, Stuart D. Bale, John W. Bonnell, Thierry Dudok de Wit, Keith Goetz, Marc Pulupa, Jasper Halekas, et al.

▶ **To cite this version:**

David M. Malaspina, Alexandros Chasapis, Peter Tatum, Chadi Salem, Stuart D. Bale, et al.. Inhomogeneous Kinetic Alfvén Waves in the Near-Sun Solar Wind. The Astrophysical Journal, 2022, 936, 10.3847/1538-4357/ac87a7 . insu-03776981

HAL Id: insu-03776981

https://insu.hal.science/insu-03776981

Submitted on 14 Sep 2022

HAL is a multi-disciplinary open access archive for the deposit and dissemination of scientific research documents, whether they are published or not. The documents may come from teaching and research institutions in France or abroad, or from public or private research centers.

L'archive ouverte pluridisciplinaire **HAL**, est destinée au dépôt et à la diffusion de documents scientifiques de niveau recherche, publiés ou non, émanant des établissements d'enseignement et de recherche français ou étrangers, des laboratoires publics ou privés.

Distributed under a Creative Commons Attribution 4.0 International License

The Astrophysical Journal, 936:128 (10pp), 2022 September 8 https://doi.org/10.3847/1538-4357/ac87a7
© 2022. The Author(s). Published by the American Astronomical Society.
OPEN ACCESS

Inhomogeneous Kinetic Alfvén Waves in the Near-Sun Solar Wind

David M. Malaspina[1,2], Alexandros Chasapis[2], Peter Tatum[1,2], Chadi Salem[3], Stuart D. Bale[3,4], John W. Bonnell[3], Thierry Dudok de Wit[5], Keith Goetz[6], Marc Pulupa[3], Jasper Halekas[7], Phyllis Whittlesey[3], Roberto Livi[3], Anthony W. Case[8], Michael L. Stevens[8], and Davin Larson[3]
[1] Astrophysical and Planetary Sciences Department, University of Colorado, 80309 Duane Physics Building, Boulder, CO 80309, USA
David.Malaspina@colorado.edu
[2] Laboratory for Atmospheric and Space Physics, University of Colorado, 1234 Innovation Drive, Boulder, CO 80303, USA
[3] Space Sciences Laboratory, University of California, 7 Gauss Way, Berkeley, CA 94720, USA
[4] Physics Department, University of California, 366 Physics North MC 7300, Berkeley, CA 94720, USA
[5] LPC2E, CNRS, CNES and University of Orléans, 3A Avenue. de la Recherche Scientifique 45071, Orléans, France
[6] School of Physics and Astronomy, University of Minnesota, Minneapolis, MN 55455, USA
[7] University of Iowa, 203 Van Allen Hall, Iowa City, IA 52242-1479, USA
[8] Harvard-Smithsonian Center for Astrophysics, 60 Garden St, Cambridge, MA 02138, USA
Received 2022 June 3; revised 2022 July 22; accepted 2022 August 5; published 2022 September 8

Abstract

Intervals of intense electromagnetic, broadband plasma waves are reported in the near-Sun solar wind. These waves are identified as kinetic Alfvén waves (KAWs), based on comparison between data and theory for their observed electric- to magnetic-field ratio, and magnetic compressibility, as a function of frequency. In contrast to KAW observations at 1 au, KAWs in the near-Sun solar wind are found to be spatially inhomogeneous, preferentially occurring where the ambient magnetic field experiences strong deviations from the Parker spiral direction, including during magnetic switchbacks and clusters of switchbacks. To the extent that turbulent fluctuations in the solar wind at small scales are characterized as KAWs, the observations reported here create an expectation that KAW-driven particle heating should also be inhomogeneous in the near-Sun solar wind, being strongest in regions of intense KAWs. Finally, a discrepancy between KAW observation and theory is identified at frequencies two decades above the frequency where kinetic effects begin to manifest, and possible origins of this discrepancy are considered.

Unified Astronomy Thesaurus concepts: Solar wind (1534); Alfven waves (23); Interplanetary turbulence (830); Space plasmas (1544); Solar magnetic fields (1503)

1. Introduction

Shear Alfvén waves become dispersive on spatial scales, where their perpendicular wavelength is on the order of the ion gyroradius (Stefant 1970; Hasegawa 1976) or the electron skin depth (Goertz & Boswell 1979), developing electric fields parallel to the background magnetic field. In plasmas with relatively weak magnetic fields and warm electrons, such that the electron thermal speed exceeds the Alfvén speed, dispersive Alfvén wave parallel electric fields are balanced by electron pressure gradients (Stasiewicz et al. 2000). These waves are referred to as kinetic Alfvén waves (KAWs).

KAWs have been observed in a wide variety of space plasmas, including within Earth's magnetosphere (magnetosheath, Gershman et al. 2017; magnetotail, Chaston et al. 2009; Ergun et al. 2015; inner magnetosphere, Chaston et al. 2014; Malaspina et al. 2015) and in the solar wind (Bale et al. 2005; Sahraoui et al. 2009; Salem et al. 2012) near 1 au. KAWs are also predicted to be active in the solar corona (Malara et al. 2019).

KAWs are thought to play a key role in the physics of the solar wind, primarily because observed properties of turbulent fluctuations below the proton gyroscale are well described as KAWs (Roberts et al. 2013; Klein et al. 2014; Wu et al. 2019; Squire et al. 2022). The presence of parallel electric fields below the ion gyroradius in KAWs enables Landau and/or transit-time damping (Gershman et al. 2017) to transfer energy from KAW fluctuations to electron heating, providing a possible path for turbulent energy dissipation in nearly collisionless plasmas like the solar wind. Theoretical paths also exist by which KAWs can produce ion heating (parallel and perpendicular; Chandran et al. 2010; Arzamasskiy et al. 2019; Isenberg & Vasquez 2019). Identifying the mechanisms that drive ion heating is critical to determining why the solar wind cools slower than adiabatic expectations as it expands (e.g., Boldyrev et al. 2020 and references therein).

Theoretical understanding of the importance of KAWs to solar wind evolution is biased by the fact that nearly all observations of KAWs in the solar wind have been made near 1 au. At that distance from the Sun, the state of the solar wind is strongly determined by its evolution during propagation from the corona to 1 au. The Parker Solar Probe spacecraft (Fox et al. 2016) traverses the near-Sun solar wind, eventually traveling as close as 0.04 au from the solar surface. From this vantage point, it is possible to observe KAWs in less evolved solar wind and thereby determine their importance to solar wind dynamics closer to the corona.

This study identifies KAWs in the near-Sun solar wind by directly comparing the properties of observed electromagnetic fluctuations with the KAW dispersion relation. KAWs are identified over large swaths of the near-Sun solar wind, and it is found that the presence and amplitude of detectable KAWs vary greatly in different regions of the solar wind. The spatial inhomogeneity of KAWs near the Sun is a strong departure

Original content from this work may be used under the terms of the Creative Commons Attribution 4.0 licence. Any further distribution of this work must maintain attribution to the author(s) and the title of the work, journal citation and DOI.

from 1 au, where KAWs are thought to pervade the solar wind in a more uniform way. The spatial inhomogeneity of KAWs near the Sun implies that their contribution to solar wind heating and/or turbulent dissipation is likewise spatially inhomogeneous.

Further, KAWs are found to preferentially occur in the presence of strong deflections of the ambient magnetic field from the nominal Parker spiral direction, including in association with switchbacks (Bale et al. 2019; Kasper et al. 2019). Switchbacks are large, spatially localized, primarily Alfvénic magnetic field fluctuations (Larosa et al. 2021) in the near-Sun solar wind, the origin of which is currently debated (Zank et al. 2020; Bale et al. 2021; Drake et al. 2021; Schwadron & McComas 2021). The association between KAWs and magnetic deflections from the Parker spiral direction allows for the possibility that intense KAWs in the near-Sun solar wind are the high-frequency extension of the large-amplitude Alfvénic fluctuations that define these magnetic deflections.

2. Data Set and Processing

This study uses data recorded by the Parker Solar Probe spacecraft (Fox et al. 2016) during its first near-Sun encounter. During this encounter, the spacecraft instruments recorded high-rate data while traversing radial distances of 55 solar radii (R_S) to $35R_S$ between 2018 October 31 and 2018 November 11. This study focuses on the first encounter because it is the only encounter where all three axes of the search coil magnetometer (SCM) function nominally.

Electric and magnetic field data recorded by the FIELDS (Bale et al. 2016; Malaspina et al. 2016; Pulupa et al. 2017) instrument suite are used, including continuously sampled time series of (i) DC-coupled electric fields along two axes in the plane of the spacecraft heat shield, (ii) three-axis DC-coupled magnetic fields from the fluxgate magnetometer (FGM), and (iii) three-axis AC-coupled magnetic fields from the SCM. These time series data sets are sampled at cadences of ~36.6, ~73.2, ~146.5, and ~293 samples s^{-1} during encounter 1, where the cadence increases as the spacecraft perihelion distance decreases. Time intervals with data sampled slower than ~36.6 samples s^{-1} are not considered in this study because data sampled slower than this rate have a Nyquist frequency too small to observe the transition to kinetic wave properties. Onboard calculated electric and magnetic field power spectra are also used, specifically the low-frequency power spectra (DC to 4687 Hz, ~27 s time averaged). Finally, total plasma density is determined from FIELDS quasi-thermal noise measurements (Moncuquet et al. 2020). When converting from differential potentials measured by the FIELDS electric field sensors to units of electric field, a fixed effective length of 2 m is assumed. This assumption has little impact on the results of this study, as discussed in Section 3. All time series data products are calibrated such that the effects of analog and digital anti-aliasing filters have been removed in ground processing.

This study uses proton and electron distribution moment data from the Solar Wind Electrons Alphas and Protons (SWEAP; Kasper et al. 2016; Case et al. 2020; Whittlesey et al. 2020) instrument suite sensors. The proton velocity is determined using data from the Solar Probe Cup (SPC). The proton core temperature perpendicular to the background magnetic field ($T_{i,\perp}$) is determined from ion Solar Probe Analyzer (SPANi) data. SPANe electron distribution function data are used, following the procedures described in Halekas et al. (2020), to estimate the electron core temperature perpendicular to the background magnetic field ($T_{e,\perp}$).

All time series FIELDS data are rotated into magnetic-field-aligned coordinates (FAC), where the slowly varying background magnetic field vector $\boldsymbol{B}$ is determined by applying a running median filter with a window of 10 s to each component of the FGM data. This window size enables analysis of electromagnetic fluctuation spectral features relative to the background magnetic field at frequencies >0.2 Hz. Ambiguity in the FAC directions perpendicular to $\boldsymbol{B}$ is resolved by defining the perpendicular FAC axes as $\mathrm{FAC}_{\perp 1} = \boldsymbol{B} \times +\hat{x}$ and $\mathrm{FAC}_{\perp 2} = \boldsymbol{B} \times (\boldsymbol{B} \times +\hat{x})$. This definition does not apply when $\boldsymbol{B}$ is exactly parallel to spacecraft $+x$, but that circumstance is vanishingly rare.

After rotation into FAC, the time series FIELDS data are processed into spectra using windowed fast Fourier transforms. The window width is fixed at ~6.9 s (corresponding to 2048 points of ~296.4 sample s^{-1} data, 1024 points of ~146.5 sample s^{-1} data, and so on). Neighboring windows have 50% overlap, and a Hanning window function is used. The resultant spectra are used to calculate power spectra and cross-spectral quantities, as discussed in Section 3.

3. Observations

Figure 1 shows plasma wave activity 5 days before and after Parker Solar Probe's encounter 1 perihelion on 2018 November 06/03:27:51 UTC. Onboard computed power spectral densities between ~20 and ~4600 Hz are shown, along with contextual background magnetic field information. Figure 1(a) shows differential electric potential fluctuation power spectral density along the V_1–V_2 axis of the FIELDS antennas. Figure 1(b) shows magnetic field fluctuation power spectral densities, summed over all three SCM axes. The local electron cyclotron frequency (f_{ce}) is shown in white for both Figures 1(a) and (b). The data in Figures 1(a) and (b) are processed such that the median (in time, at each frequency) power spectral density from each 15 minutes is plotted. This median processing removes the large-amplitude, transient signatures of dust impacts (Malaspina et al. 2020; Page et al. 2020; Szalay et al. 2020), while retaining large-scale plasma wave behavior. The monochromatic features near 100 Hz in Figure 1(b) are the magnetic signatures of the spacecraft reaction wheels. Figure 1(c) shows $\pm|B|$ in black and the radial magnetic field component (B_R) in blue, both down-sampled to 4 samples s^{-1}. Nonradial magnetic field intervals, including magnetic switchbacks, are characterized by deviations of B_R from $|B|$.

Broadband electromagnetic wave power is evident from ~20 to ~300 Hz, never exceeding f_{ce}, throughout the encounter. The occurrence of broadband waves is observed to be correlated with switchback patches (Bale et al. 2021; Fargette et al. 2021), such that larger-amplitude waves occur most often in the presence of switchback patches.

To examine the potential correlation between the identified broadband wave activity and magnetic deflections, including switchbacks, more closely, Figure 2 focuses on the first 12 hr of 2018 November 05 (any interval from encounter 1 shows similar behavior). Figures 2(a), (b), and (c) have the same format as Figures 1(a), (b), and (c), except that the power spectral densities shown are as sampled by FIELDS instead of median-processed. Figure 2(d) shows the SCM power spectral density, summed from 20 to 200 Hz. This metric tracks the relative intensity of the broadband waves.

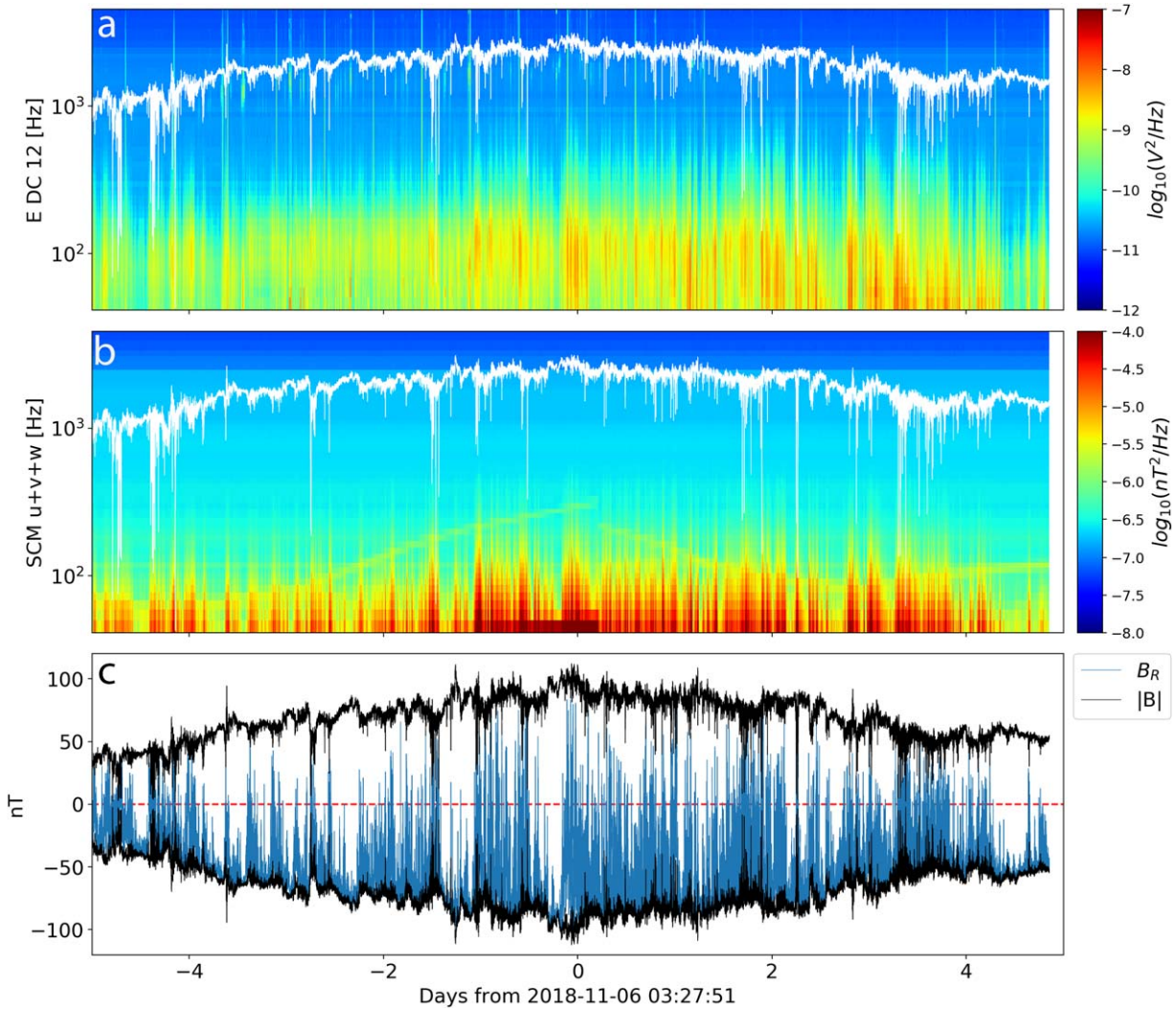

Figure 1. Plasma wave activity between ∼20 and ∼4600 Hz and magnetic field context from solar encounter 1. (a) Differential voltage power spectral density on channel V_{12}. (b) Magnetic field power spectral densities, summed over all three search coil axes. (c) 4 sample s^{-1} magnetic field fluctuations. $\pm |B|$ is shown in black, and the radial magnetic field component B_R is shown in blue.

On this several-hour timescale, individual switchbacks can be discerned. The wave intensity metric (bottom panel) qualitatively tracks strong deviations of B_R from $|B|$. That is, broadband wave power spectral density increases when the background magnetic field becomes nonradial, including during switchbacks. The correlation is not linear, in that the most intense waves do not always occur with the most nonradial magnetic fields. For example, the peak in summed power spectral density near 3 hr, which occurs with a background magnetic field that is roughly perpendicular to radial, has a larger amplitude than the peak that occurs just after 4 hr, which occurs during a nearly complete reversal of the ambient magnetic field.

From Figure 2, it is also clear that broadband electromagnetic wave activity is present throughout the duration of any given switchback (e.g., just after 2 hr, just after 4 hr, just before 10 hr), and not only at the switchback boundaries, where swings in the ambient magnetic field direction are most abrupt and other wave modes are known to be active (Krasnoselskikh et al. 2020; Larosa et al. 2021).

Electric and magnetic field spectra calculated from the continuous waveform data (as described in Section 2) are used to identify these broadband waves as KAWs. Figure 3 shows spectral data from one ∼6.9 s interval on 2018 November 5, near 02:17:46 UTC. Figure 3(a) shows the ratio of electric to magnetic field fluctuations perpendicular to the background magnetic field $|\delta E_\perp|/|\delta B_\perp|$, normalized to the local Alfvén speed $v_A = |B|/\sqrt{\mu_0 m_p n_p}$, as a function of spacecraft-frame frequency. Here m_p is the mass of a proton and n_p is the proton density, assumed to be approximately equal to the measured total electron density ($n_p \approx n_e$). FGM data are used at 4 Hz and below (blue), while SCM data are used above 4 Hz (orange). This frequency (4 Hz) approximately corresponds to the crossover point between the noise floors of the FGM and SCM sensors (Bowen et al. 2020). The magnetic field power spectra and the calculated fluctuation ratio are smoothly continuous across 4 Hz. DC-coupled electric field data are used for all frequencies shown. A horizontal dashed line shows where $|\delta E_\perp|/|\delta B_\perp| = v_A$, the condition expected for a long-wavelength shear Alfvén wave. For some spectral intervals, $|\delta E_\perp|/|\delta B_\perp|$ is shifted above v_A for frequencies below ∼1 Hz. It is assumed that this shift is due to variability in the effective electrical length of the FIELDS antennas in response to changing plasma conditions. Shifts between 1× and 4× are

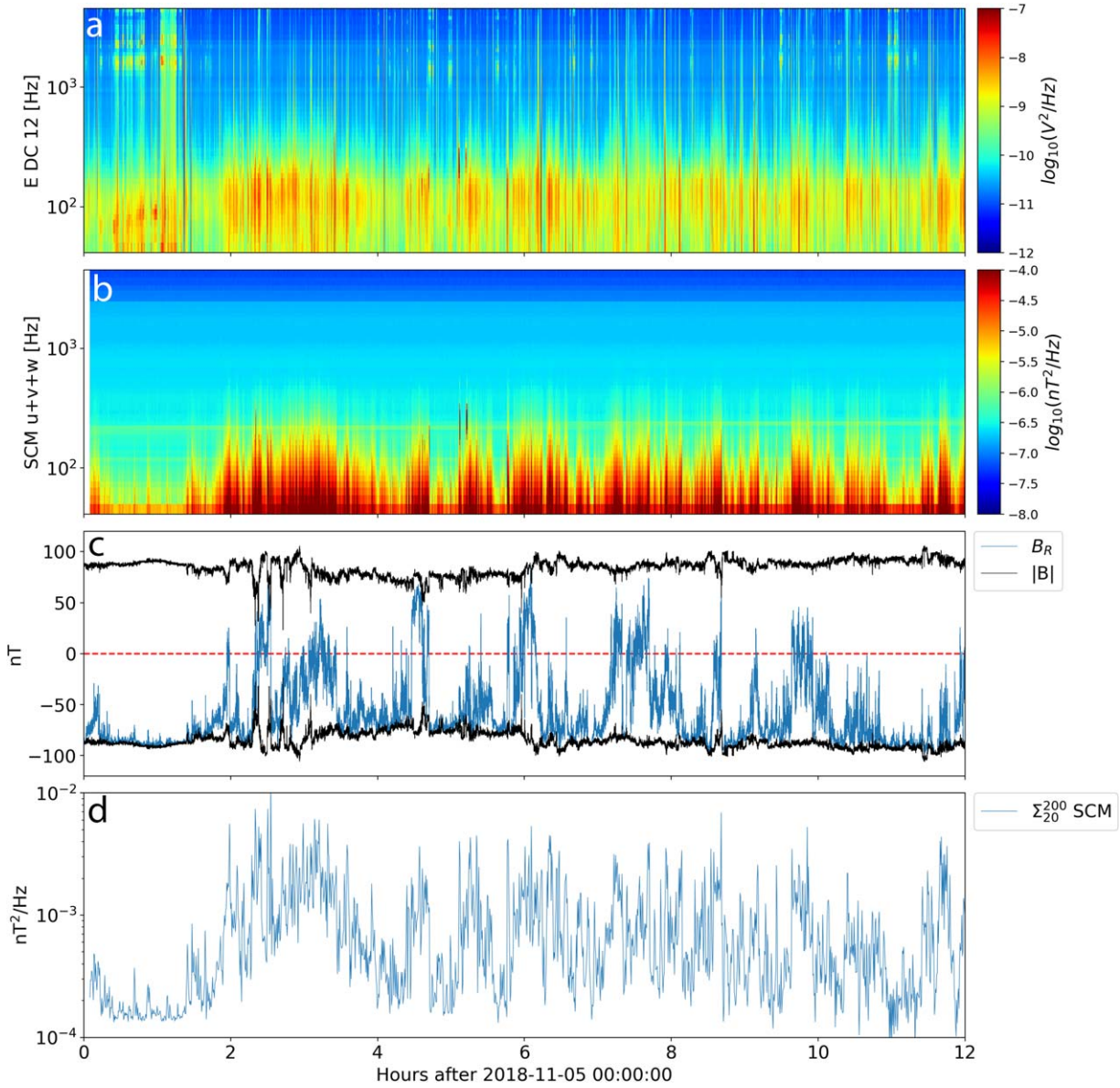

Figure 2. Plasma wave activity between ~20 and ~4600 Hz and magnetic field context from a 12 hr interval during solar encounter 1. (a–c) Same as the corresponding panels in Figure 1. (d) Time series of the magnetic power spectral density, summed from 20 to 200 Hz.

required, consistent with Mozer et al. (2020) analysis of FIELDS effective electrical length variability. For these spectra, the entire $|\delta E_\perp|/|\delta B_\perp|$ spectrum is shifted in amplitude such that the lowest-frequency portion (below ~1 Hz) is centered on v_A.

Figure 3(b) shows the cross-spectral coherence (C) between δE and δB fluctuations at each frequency, defined as follows:

$$C = \sqrt{\frac{\langle \mathrm{FT_1 FT_2^*} \rangle \langle \mathrm{FT_1^* FT_2} \rangle}{\langle \mathrm{FT_1 FT_1^*} \rangle \langle \mathrm{FT_2 FT_2^*} \rangle}}. \quad (1)$$

Here FT_1 and FT_2 are the Fourier transforms of signals 1 and 2, respectively, and angle brackets denote ensemble averages. For this analysis, mean-smoothing in frequency space (7-bin window, centered on each frequency) is used in place of the ensemble averages in time. Mean-smoothing in time was also examined, but no significant differences in any of the figures presented in this work were found (see Section 4). Coherence is calculated for both FAC perpendicular dimensions as C_{12} for signal $1 = \delta E_{\perp 1}$ and signal $2 = \delta B_{\perp 2}$ and as C_{21} for signal $1 = \delta E_{\perp 2}$ and signal $2 = \delta B_{\perp 1}$. C_{12} is used for coherence for spectra where $\delta B_{\perp 2} > \delta B_{\perp 1}$, and C_{21} is used where $\delta B_{\perp 1} > \delta B_{\perp 2}$. A horizontal dashed line indicates 0.8.

Figure 3(c) shows the same data as Figure 3(a), using black circles, but only includes data points with high coherence (>0.8) between $\delta E_\perp$ and $\delta B_\perp$. A red dashed line indicates the theoretical KAW $|\delta E_\perp|/|\delta B_\perp|$ ratio given by Stasiewicz et al. (2000) and reproduced as follows:

$$\frac{|\delta E_\perp|}{|\delta B_\perp|} = v_A \frac{(1 + k_\perp^2 \rho_i^2)}{\sqrt{1 + k_\perp^2 (\rho_s^2 + \rho_i^2)}}. \quad (2)$$

Here the proton gyroradius is $\rho_i = (m_p v_{\mathrm{thp},\perp})/(q_p|B|)$, where the proton thermal speed is determined from the perpendicular proton temperature ($T_{p,\perp}$) as $v_{\mathrm{thp},\perp} = \sqrt{2k_B T_{p,\perp}/m_p}$. The proton gyroradius at the electron temperature is $\rho_s = m_p v_{\mathrm{ths},\perp}/q_p|B|$, where the relevant thermal speed is determined from the perpendicular electron temperature ($T_{e,\perp}$) as $v_{\mathrm{ths},\perp} = \sqrt{2k_B T_{e,\perp}/m_p}$. The charge

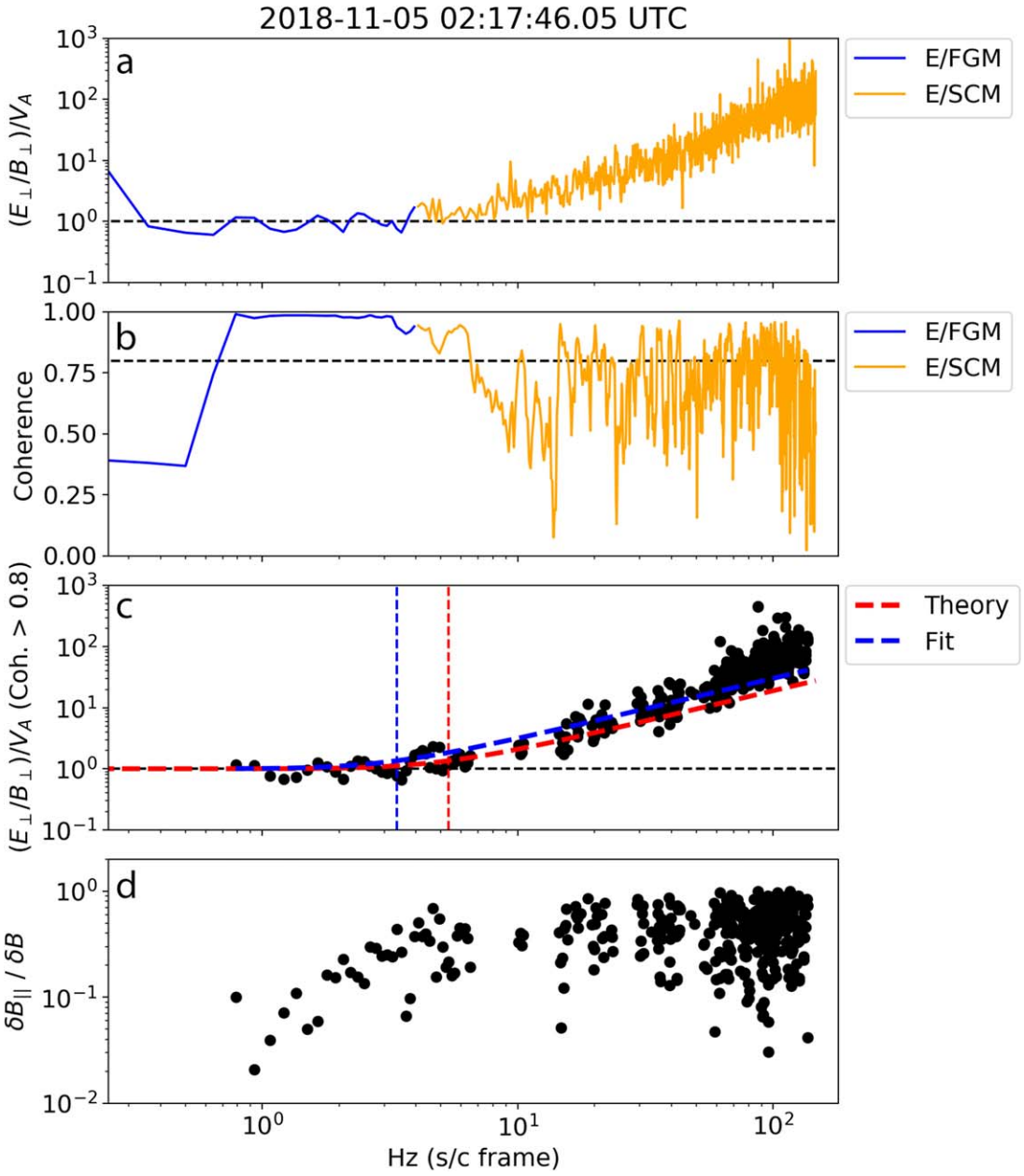

Figure 3. Representative example of spectral processing and features for a ~6.9 s window containing KAWs. (a) Ratio of electric to magnetic fluctuations perpendicular to the background magnetic field direction, normalized to the local Alfvén speed. The overall level is adjusted to compensate for variable effective electrical length of the FIELDS antennas (see text). (b) Coherence between perpendicular fluctuations in the electric and magnetic field. (c) Black circles contain the same data as in panel (a), but only for points with coherence >0.8. The red dashed curve shows a prediction from KAW theory; the blue dashed curve shows a best-fit curve (see text for details). Vertical red and blue dashed lines show the "knee" frequency, where the wave fluctuations begin to show kinetic properties. (d) The ratio of magnetic field fluctuations parallel and perpendicular to the slowly varying background magnetic field. All quantities are shown as a function of spacecraft-frame frequency.

on a proton is q_p, and Boltzmann's constant is k_B. The KAW perpendicular wavenumber is $k_\perp$.

For this theoretical ratio, it is assumed that the waves are oblique such that $k_\perp >> k_\parallel$, and it is assumed that Doppler shift dominates the observed frequencies such that $k_\perp \approx (2\pi f)/v_{t,\perp}$, where $v_{t,\perp}$ is the component of the proton rest-frame velocity, relative to the spacecraft, perpendicular to the background magnetic field direction. The Parker Solar Probe spacecraft velocity ($\boldsymbol{v}_{sc}$) can be comparable to the solar wind velocity ($\boldsymbol{v}_{sw}$); therefore, $\boldsymbol{v}_t$ is defined as $\boldsymbol{v}_t = \boldsymbol{v}_{sw} + \boldsymbol{v}_{sc}$.

The above assumptions, combined with measurements of $T_{p,\perp}$ from SPANi, v_{sw} from SPC, $T_{e,\perp}$ from SPANe, $|B|$ from the FGM, and n_e from the FIELDS QTN data, provide all terms on the right-hand side of Equation (2), and the resulting theoretical curve is plotted as the red dashed line in Figure 3(c).

The data qualitatively agree with the theoretical KAW curve, clustering near v_A at low frequencies and becoming more electrostatic at high frequencies, with nearly the theoretical spectral slope. The frequency (f_{knee}) of the knee in the theoretical KAW curve (where $|\delta E_\perp|/(v_A|\delta B_\perp|)$ exceeds 1) is indicated by the vertical red dashed line.

One can see that the measured electric-to-magnetic field ratio is farther from the theoretical curve at higher frequencies. The data are above the theoretical curve by a factor of ~2 near

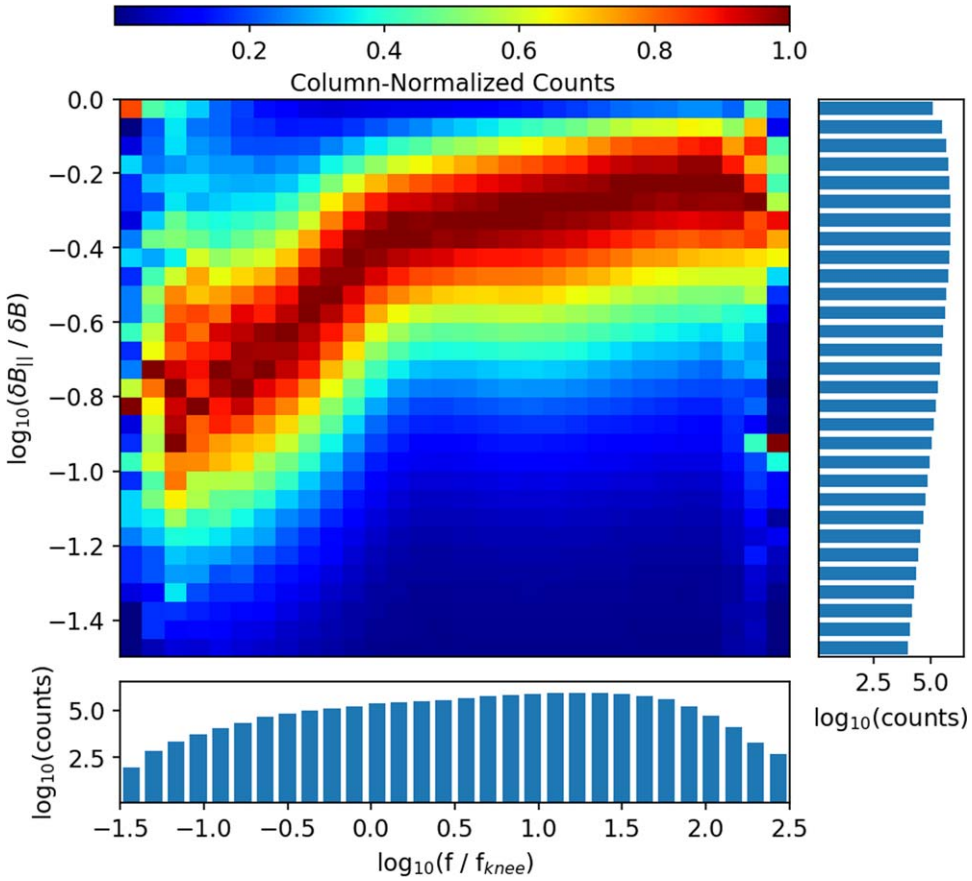

Figure 4. Two-dimensional histogram of the ratio of magnetic field fluctuations parallel and perpendicular to the slowly varying background magnetic field as a function of spacecraft-frame frequency, normalized to the "knee" frequency where the waves begin to show kinetic properties. Each column of the histogram has been normalized to the largest value in that column. Horizontal and vertical histograms show the number of data points in each column and row, respectively.

30 Hz and by a factor of ∼5 near 100 Hz. The origin of this discrepancy is not yet clear, but possibilities are discussed in Section 4.

In addition to the theoretical curve, a best-fit curve (blue dashed line) is also plotted. The best-fit curve follows Equation (3), where a fit parameter α is inserted. The purpose of α is to allow for large uncertainties in $T_{p,\perp}$, $T_{e,\perp}$, and $v_{\rm sw}$ (which translate into uncertainties in $k_\perp$, ρ_i, and ρ_s), associated with the SPANi and SPC field-of-view limitations during encounter 1. Specifically, the solar wind beam is not completely within the SPANi field of view during encounter 1, and SPC moments are derived from a unidirectional cut through the full distribution function.

It is found that the slope of the $|\delta E_\perp|/(v_{\rm A}|\delta B_\perp|)$ data steepens with frequency in a way that cannot be accounted for by particle distribution moment uncertainties, insofar as they are quantified by α. The value of $f_{\rm knee}$ for the best-fit curve is indicated by a vertical blue dashed line. The best-fit curve uses data <40 Hz and least-squares fitting to determine the value of α. Values for α are found to fluctuate between 0.5 and 3 over the course of the encounter. The measured electric- to magnetic-field fluctuation ratio matches or exceeds the best-fit curve near 100 Hz:

$$\frac{|\delta E_\perp|}{|\delta B_\perp|} = v_{\rm A}\frac{(1+\alpha^2 k_\perp^2\rho_i^2)}{\sqrt{1+\alpha^2 k_\perp^2(\rho_s^2+\rho_i^2)}}. \quad (3)$$

Finally, Figure 3(d) shows the ratio of magnetic field fluctuations along the background magnetic field ($\delta B_\parallel$) to fluctuations of the total magnetic field (δB), as a function of frequency. Only data with coherence >0.8 are considered. This quantity is calculated to evaluate the possibility that the observed fluctuations may be whistler mode (Chaston et al. 2009; Rosenlof & Reid 2009). Many observational studies at 1 au concluded that similar fluctuations below the ion gyroscale are more consistent with KAWs than whistler mode (Salem et al. 2012; Chen et al. 2013; Roberts et al. 2013). Because the near-Sun waves examined here show different spatial distribution than those at 1 au, it is important to test whether these waves are KAW or whistler mode.

Similar to 1 au KAW observations (Salem et al. 2012) and predictions for KAWs (Rosenlof & Reid 2009), the quantity $\delta B_\parallel/\delta B$ is found to be small at low frequencies, increase until the frequency where Alfvén waves become dispersive, and then remain approximately flat with increasing frequency, staying below 1. This behavior supports the identification of these fluctuations as KAWs. However, there is significant scatter in $\delta B_\parallel/\delta B$ for any given ∼6.9 s spectra. This issue is addressed by Figure 4.

The data processing shown in Figure 3 is applied to every ∼6.9 s window for the full encounter 1 interval. For each time window, the coherence between $\delta E_\perp$ and $\delta B_\perp$ is calculated and fits are made to the high-coherence data. The KAW theory and KAW best-fit knee frequencies ($f_{\rm knee}$) are determined as described above. In addition, $\delta B_\parallel/\delta B$ is calculated for each time window. A given time window is determined to contain a KAW observation if the following criteria are met: (i) >50% of

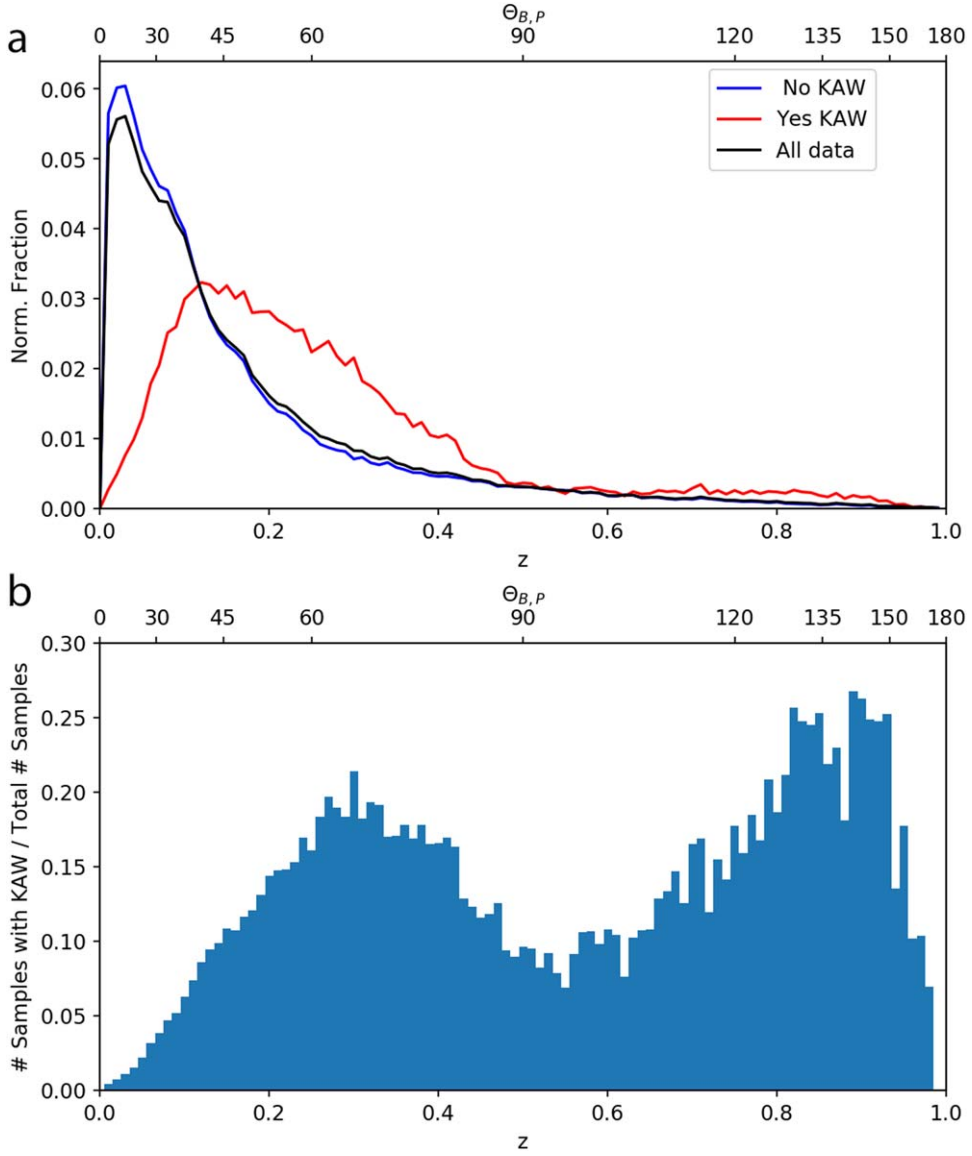

Figure 5. (a) Occurrence histograms of ∼6.9 s intervals with (red) or without (blue) identified KAWs, and all data (black) as a function of the normalized magnetic field deflection parameter z (see text). Each histogram is normalized by the total number of counts contained in that histogram. The three-dimensional angle between the background magnetic field and the Parker spiral direction that defines z is given for reference on the top horizontal axis. (b) The fraction of all data samples with identified KAW in each z bin.

data points in the FGM frequency range (0.2–4 Hz) have high coherence (>0.8), (ii) >30% of data points in the SCM frequency range (>4 Hz) have high coherence (>0.8), and (iii) the KAW fit parameter α is in the range of 0.5–3. The resulting two data sets, time windows with KAWs and time windows without KAWs, are used in the following analysis. Using these criteria to identify KAWs, 12.1% of encounter 1 (sunward of $55R_S$) is found to contain contain KAWs.

The data in Figure 4 show that the fluctuations under study here are consistent with KAWs rather than whistler-mode waves. Figure 4 shows a two-dimensional histogram of $\delta B_{\parallel}/\delta B$ as a function of $(f/f_{\rm knee})$. Here $f_{\rm knee}$ is determined using the best-fit curves, and only data with high coherence from time windows with KAWs are considered. The two-dimensional histogram data are normalized, per column, by the maximum number of observations in that column. The horizontal and vertical histograms show the total number of observations in each row and column, showing that most rows and columns have several hundred thousand data points. The composite trend in Figure 4 is entirely consistent with KAWs, but not with whistler-mode fluctuations (Rosenlof & Reid 2009; Salem et al. 2012): $\delta B_{\parallel}/\delta B$ is small at low wavenumbers (equivalent to spacecraft-frame frequencies with the Doppler shift approximation considered here), then increases with frequency until the waves become dispersive ($f_{\rm knee}$), and then remains approximately flat. The magnetic compressibility of whistler-mode fluctuations is expected to show the highest values at low frequencies, decrease with frequency until the waves become dispersive, and then remain flat at a relatively low value (Rosenlof & Reid 2009). Given this evidence, the broadband electromagnetic waves studied here are identified as KAWs rather than whistler-mode waves.

Finally, Figure 5 explores the association between KAW observations and nonradial magnetic fields suggested by Figures 1 and 2. Figure 5(a) shows three histograms, indicating the number of observations as a function of normalized

magnetic deflection from a nominal Parker spiral direction (z), where z is defined according to Dudok de Wit et al. (2020):

$$z = \frac{1}{2}(1 - \cos\theta_{B,P}). \quad (4)$$

Here $\theta_{B,P}$ is the three-dimensional angle between the measured magnetic field vector direction and the nominal Parker spiral magnetic field direction. The nominal Parker spiral direction for each observation time window is assumed to be in the R–T plane, with a value determined using a solar rotation frequency of 25.38 days and the median radial solar wind speed measured by SPC during each time window. The median magnetic field vector, in RTN coordinates, for each time window, is also used to determine $\theta_{B,P}$. The histogram in red (blue) includes all time windows during encounter 1 where KAWs were (were not) detected, using the detection criteria defined above. Each histogram is normalized to the total number of observations in that histogram. The histogram in black shows all data (KAWs detected plus KAWs not detected). At low z values, the black curve is below the blue curve. This is consistent with fractionally fewer KAW events at low z. Near $z = 0.3$, the black curve is above the blue curve. This is consistent with fractionally more KAW events at $z \approx 0.3$ compared to "no KAW" events. The relatively small deviations between the blue and black curves are expected considering that only 12.1% of the full data set is found to contain KAWs.

Figure 5(b) uses the same data as Figure 5(a) but plots the fraction of all data samples with identified KAWs for each z bin. The data in Figure 5(b) show that up to 20% of all intervals with $\theta_{B,P} \sim 60°$ contain KAWs. The fractional occurrence of KAWs dips to ~10% near $\theta_{B,P} \sim 90°$ and climbs to its highest values at large z (~25% near $\theta_{B,P} \sim 140°$). The fractional occurrence of KAWs is lowest at small z (<5% near $\theta_{B,P} < 30°$). These data show that KAWs are more likely to occur when the magnetic field is deflected away from the Parker spiral than in the absence of such deflections.

Interestingly, the fractional occurrence rate in Figure 5(b) dips near $\theta_{B,P} \approx 90°$. This indicates that observation of KAWs is not dominantly determined by Doppler shift (which would produce a KAW observation maximum near $\theta_{B,P} \approx 90°$) and is not dominantly determined by the orientation of the FIELDS antennas with respect to the ambient magnetic field (which should produce a KAW observation maximum near $\theta_{B,P} \approx 0°$, where $|\delta E_\perp|$ is best measured).

This statistical result is entirely consistent with the qualitative correlation observed in Figures 1 and 2: KAWs with strong enough amplitudes to be identified preferentially occur in regions of non-Parker spiral magnetic fields. During encounter 1, these regions are spatially inhomogeneous and are defined by switchbacks (Bale et al. 2019; Dudok de Wit et al. 2020). This is in contrast to 1 au observations, where KAWs are considered to pervade the solar wind, regardless of magnetic field deflection (Salem et al. 2012; Chen et al. 2013; Roberts et al. 2013).

4. Discussion

From Figure 3, one can see that the observed fluctuations are more electrostatic than predicted by KAW theory, or a best-fit curve with one free parameter, at high frequencies (~100 Hz). This feature is consistently observed throughout encounter 1, across values of $\theta_{B,P}$ and v_{sw}. While the origin of this feature is unclear, several possibilities are discussed here. Each of these should be further explored in future work.

First, measurement uncertainties in $T_{p,\perp}$ and $T_{e,\perp}$ and/or v_{sw} due to field of view challenges related to the Parker Solar Probe heat shield lead to uncertainties in $k_\perp$, ρ_i, and ρ_s. The fit parameter α was introduced in an attempt to control for these uncertainties. Yet the slope of the $|\delta E_\perp|/(v_A|\delta B_\perp|)$ data steepens with frequency, which cannot be accounted for by the defined α.

Second, it is possible that spacecraft plasma sheath effects impose a frequency-dependent gain on the electric field measurements that is not compensated by FIELDS data calibrations. This explanation is difficult to reconcile with the data, as the transition from resistive to capacitive coupling of antennas to the plasma through the sheath often lowers the gain of E with increasing frequency (Bale et al. 2008; Hartley et al. 2022). The data in Figure 3 show the opposite behavior. Still, enhancement of electric field gain due to sheath effects is possible and has been reported in prior studies (Hartley et al. 2022).

A third possibility is that the magnetic fluctuations are approaching the SCM noise floor above ~40 Hz. To explore this, an additional criterion was tested where spectral analysis was carried out only if the SCM fluctuations >40 Hz showed a signal-to-noise ratio greater than 5. The excess $|\delta E_\perp|/(v_A|\delta B_\perp|)$ near 100 Hz persisted in spite of this additional criterion.

A fourth possibility is that the excess electrostatic fluctuations represent a physical departure from Equation (2). Equation (2) is derived by Stasiewicz et al. (2000) under the assumption that the plasma-frame frequency of the KAWs (ω) is less than the ion-cyclotron frequency (ω_{ci}). Additional terms that scale like $(1 - \omega^2/\omega_{ci}^2)$ are introduced when $\omega > \omega_{ci}$. In this regime, the ratio $\delta E_\perp/\delta B_\perp$ is expected to be reduced at higher frequencies (as shown in Salem et al. 2012). Due to signal-to-noise ratio limitations of 1 au solar wind measurements, prior observations of KAWs in the solar wind extend only one frequency decade or less past the ion gyrofrequency. Near the Sun, high KAW amplitudes enable observations two or more decades past the ion gyrofrequency, enabling more direct tests of whether solar wind electromagnetic fluctuations maintain KAW properties at frequencies more than a decade above the ion gyrofrequency.

In this analysis, it was assumed that the Doppler shift term ($k_\perp v_\perp$) is much larger than the plasma-frame frequency of the KAW (ω_p). A fifth possibility for the electrostatic excess at high frequencies compared to KAW theory is that this Doppler shift assumption breaks down at high frequencies.

To test this possibility, the median of the difference between data and KAW theory (Equation (2)) at frequencies >40 Hz was examined as a function of $v_\perp/v_A$, for all Yes-KAW events (not shown). The data suggest a weak trend, where higher values of $v_\perp/v_A$ may be associated with lower data–theory differences, but the scatter in values of data–theory difference exceeds an order of magnitude at all values of $v_\perp/v_A$. Therefore, we conclude that breakdown of the strict Doppler shift assumption may play some role in the extra electrostatic power but is unlikely to be the dominant effect.

For completeness, cross-spectral coherence was also calculated by using a mean-smoothing in time (seven spectral intervals of ~6.9 s each, centered on each ~6.9 s spectral interval) instead of the mean-smoothing in frequency described

above. Frequency-smoothing resulted in a larger percentage of spectral intervals during encounter 1 identified as containing KAW (12.1%) compared to time-smoothing (8.2%). A decrease is expected given that time-smoothing will average KAW intervals with adjacent non-KAW intervals, reducing δE to δB coherence, resulting in fewer intervals that exceed the coherence-based criteria for identification as KAWs. Otherwise, the choice of smoothing dimension is not found to impact the results of this study.

This study demonstrates that KAWs are inhomogeneously distributed in the near-Sun solar wind. To the extent that KAW fluctuations dissipate turbulent energy and result in the heating of plasma (parallel or perpendicular to $\boldsymbol{B}$), this heating is also expected to be spatially inhomogeneous and should be more emphatic in regions where the magnetic field more often deviates from the Parker spiral direction, including switchbacks.

Several studies report no significant difference in proton core temperatures inside and outside of individual switchbacks (Woolley et al. 2020; Martinovic et al. 2021), though other studies report enhanced proton temperatures (parallel and/or perpendicular) related to clusters of switchbacks (Bale et al. 2021; Woodham et al. 2021). While the association between electron core temperatures and switchbacks has not yet been investigated in detail, encounter-long electron observations suggest no strong electron temperature variation in the presence of switchbacks (Halekas et al. 2020). Conversely, quiescent solar wind regions, which are devoid of switchbacks, do not show significant variability in ion or electron temperatures (Short et al. 2022) across their boundaries.

If KAWs play a strong role in turbulent dissipation, and enhanced KAWs indicate enhanced transfer of energy from large-scale Alfvénic fluctuations to particle heating, why is it difficult to observe a clear correlation between times of magnetic deflection (including switchbacks) and solar wind core particle heating? Further, what physical process determines the probability of observing KAWs in association with a given magnetic deflection (Figure 5(b))? These are important questions to address while seeking to determine the role that KAW may play in solar wind core particle heating.

This study demonstrates that identifiable KAWs are most likely to be observed when the background magnetic field deviates from the Parker spiral direction (Figure 5(b)), including during switchbacks. Further, KAW amplitudes are found to be modulated by the presence of switchback magnetic fields (Figure 2) and clusters of switchback magnetic fields (Figure 1).

Considering that switchbacks have been identified as large-scale, mostly Alfvénic fluctuations (Larosa et al. 2021), their association with enhanced KAWs is entirely consistent with studies in other regions of space. Intense KAWs are observed to coincide with large-scale Alfvénic fluctuations in the magnetosheath (Gershman et al. 2017), in the magnetotail (Chaston et al. 2009; Ergun et al. 2015), and in the inner magnetosphere (Malaspina et al. 2015). This similarity to prior observations, as well as the smooth transition from shear Alfvén to KAW properties (Figure 3), strongly suggests that the near-Sun KAWs reported here are small-scale extensions (or decay products; Tenerani et al. 2021) of the large-scale Alfvénic fluctuations that define magnetic switchbacks. If this is true, then the spatial inhomogeneity of intense KAWs is a natural consequence of the spatial inhomogeneity of large-scale Alfvénic fluctuations in the near-Sun solar wind.

5. Conclusion

This study has demonstrated the existence of intense intervals of KAWs in the near-Sun solar wind. It has been shown that intervals of intense KAWs are spatially inhomogeneous, preferentially occurring where the background magnetic field is significantly deflected from the Parker spiral direction, including in the presence of individual magnetic switchbacks and clusters of switchbacks. If KAWs result in significant solar wind particle heating, one would expect to observe differences in such heating inside and outside of regions where the magnetic field deviates from the Parker spiral, but the opposite is reported by several existing studies, at least for particle distribution function core heating. Finally, the observed KAWs are found to be more electrostatic than predicted by KAW theory at frequencies two decades above the frequency where kinetic wave properties begin to appear. Instrumental and physical possibilities for this discrepancy were discussed, but future work is required to provide a definitive explanation.

Parker Solar Probe was designed, was built, and is now operated by the Johns Hopkins Applied Physics Laboratory as part of NASA's Living with a Star (LWS) program (contract NNN06AA01C). Support from the LWS management and technical team has played a critical role in the success of the Parker Solar Probe mission. T.D. acknowledges support by CNES.

ORCID iDs

David M. Malaspina https://orcid.org/0000-0003-1191-1558
Alexandros Chasapis https://orcid.org/0000-0001-8478-5797
Chadi Salem https://orcid.org/0000-0002-6536-1531
Stuart D. Bale https://orcid.org/0000-0002-1989-3596
John W. Bonnell https://orcid.org/0000-0002-0675-7907
Thierry Dudok de Wit https://orcid.org/0000-0002-4401-0943
Keith Goetz https://orcid.org/0000-0003-0420-3633
Marc Pulupa https://orcid.org/0000-0002-1573-7457
Jasper Halekas https://orcid.org/0000-0001-5258-6128
Phyllis Whittlesey https://orcid.org/0000-0002-7287-5098
Roberto Livi https://orcid.org/0000-0002-0396-0547
Anthony W. Case https://orcid.org/0000-0002-3520-4041
Michael L. Stevens https://orcid.org/0000-0002-7728-0085
Davin Larson https://orcid.org/0000-0001-5030-6030

References

Arzamasskiy, L., Kunz, M. W., Chandran, B. D. G., & Quataert, E. 2019, ApJ, 879, 53
Bale, S. D., Badman, S. T., Bonnell, J. W., et al. 2019, Natur, 576, 237
Bale, S. D., Goetz, K., Harvey, P. R., et al. 2016, SSRv, 204, 49
Bale, S. D., Horbury, T. S., Velli, M., et al. 2021, ApJ, 923, 174
Bale, S. D., Kellogg, P. J., Mozer, F. S., Horbury, T. S., & Reme, H. 2005, PhRvL, 94, 215002
Bale, S. D., Ullrich, R., Goetz, K., et al. 2008, SSRv, 136, 529
Boldyrev, S., Forest, C., & Egedal, J. 2020, PNAS, 117, 9232
Bowen, T. A., Bale, S. D., Bonnell, J. W., et al. 2020, JGRA, 125, e27813
Case, A. W., Kasper, J. C., Stevens, M. L., et al. 2020, ApJS, 246, 43
Chandran, B. D. G., Li, B., Rogers, B. N., Quataert, E., & Germaschewski, K. 2010, ApJ, 720, 503
Chaston, C. C., Bonnell, J. W., Wygant, J. R., et al. 2014, GeoRL, 41, 209
Chaston, C. C., Johnson, J. R., Wilber, M., et al. 2009, PhRvL, 102, 015001
Chen, L., Thorne, R. M., Li, W., & Bortnik, J. 2013, JGRA, 118, 1074

Drake, J. F., Agapitov, O., Swisdak, M., et al. 2021, A&A, 650, A2
Dudok de Wit, T., Krasnoselskikh, V. V., Bale, S. D., et al. 2020, ApJS, 246, 39
Ergun, R. E., Goodrich, K. A., Stawarz, J. E., Andersson, L., & Angelopoulos, V. 2015, JGRA, 120, 1832
Fargette, N., Lavraud, B., Rouillard, A. P., et al. 2021, ApJ, 919, 96
Fox, N. J., Velli, M. C., Bale, S. D., et al. 2016, SSRv, 204, 7
Gershman, D. J., F-Viñas, A., Dorelli, J. C., et al. 2017, NatCo, 8, 14719
Goertz, C. K., & Boswell, R. W. 1979, JGR, 84, 7239
Halekas, J. S., Whittlesey, P., Larson, D. E., et al. 2020, ApJS, 246, 22
Hartley, D. P., Christopher, I. W., Kletzing, C. A., et al. 2022, JGRA, 127, e2022JA030369
Hasegawa, A. 1976, JGR, 81, 5083
Isenberg, P. A., & Vasquez, B. J. 2019, ApJ, 887, 63
Kasper, J. C., Abiad, R., Austin, G., et al. 2016, SSRv, 204, 131
Kasper, J. C., Bale, S. D., Belcher, J. W., et al. 2019, Natur, 576, 228
Klein, K. G., Howes, G. G., TenBarge, J. M., & Podesta, J. J. 2014, ApJ, 785, 138
Krasnoselskikh, V., Larosa, A., Agapitov, O., et al. 2020, ApJ, 893, 93
Larosa, A., Krasnoselskikh, V., Dudok de Wit, T., et al. 2021, A&A, 650, A3
Malara, F., Nigro, G., Valentini, F., & Sorriso-Valvo, L. 2019, ApJ, 871, 66
Malaspina, D. M., Claudepierre, S. G., Takahashi, K., et al. 2015, GeoRL, 42, 9203
Malaspina, D. M., Ergun, R. E., Bolton, M., et al. 2016, JGRA, 121, 5088
Malaspina, D. M., Szalay, J. R., Pokorny, P., et al. 2020, ApJ, 892, 115
Martinovic, M. M., Klein, K. G., Huang, J., et al. 2021, ApJ, 912, 28
Moncuquet, M., Meyer-Vernet, N., Issautier, K., et al. 2020, ApJS, 246, 44
Mozer, F. S., Agapitov, O. V., Bale, S. D., et al. 2020, JGRA, 125, e27980
Page, B., Bale, S., Bonnell, J. W., et al. 2020, ApJ, 246, 51
Pulupa, M., Bale, S. D., Bonnell, J. W., et al. 2017, JGRA, 122, 2836
Roberts, O. W., Li, X., & Li, B. 2013, ApJ, 769, 58
Rosenlof, K. H., & Reid, G. C. 2009, JGRA, 114, A12105
Sahraoui, F., Goldstein, M. L., Robert, P., & Khotyaintsev, Y. 2009, PhRvL, 102, 231102
Salem, C. S., Howes, G. G., Sundkvist, D., et al. 2012, ApJL, 745, L9
Schwadron, N. A., & McComas, D. J. 2021, ApJ, 909, 95
Short, B., Malaspina, D., Halekas, J., et al. 2022, ApJ, in press
Squire, J., Meyrand, R., Kunz, M. W., et al. 2022, NatAs, 6, 715
Stasiewicz, K., Bellan, P., Chaston, C., et al. 2000, SSRv, 92, 423
Stefant, R. J. 1970, PhFl, 13, 440
Szalay, J. R., Pokorný, P., Bale, S., et al. 2020, ApJ, 246, 27
Tenerani, A., Sioulas, N., Matteini, L., et al. 2021, ApJL, 919, L31
Whittlesey, P. L., Larson, D. E., Kasper, J. C., et al. 2020, ApJS, 246, 74
Woodham, L. D., Horbury, T. S., Matteini, L., et al. 2021, A&A, 650, L1
Woolley, T., Matteini, L., Horbury, T. S., et al. 2020, MNRAS, 498, 5524
Wu, H., Verscharen, D., Wicks, R. T., et al. 2019, ApJ, 870, 106
Zank, G. P., Nakanotani, M., Zhao, L.-.-L.-., Adhikari, L., & Kasper, J. 2020, ApJ, 903, 1